Journal of Applied Fluid Mechanics, Vol. 17, No. 12, pp. 2563-2578, 2024.
Available online at www.jafmonline.net, ISSN 1735-3572, EISSN 1735-3645.
https://doi.org/10.47176/jafm.17.12.2773

Sweep Optimization to Reduce Aerodynamic Loss in a Transonic Axial Compressor with Upstream Boundary Layer Ingestion

T. Pan[1,2,3], K. Shi[2,3,4], H. Lu[2,3,4†], J. Zhang[4] and Q. Li[4,5]

[1.] *Research Institute of Aero-Engine, Beihang University, Beijing, 100191, China*
[2.] *National Key Laboratory of Science and Technology on Aero-Engine Aero-Thermodynamics, Beihang University, Beijing, 100191, China*
[3.] *Collaborative Innovation Center for Advanced Aero-Engine, Beihang University, Beijing, 100191, China*
[4.] *School of Energy and Power Engineering, Beihang University, Beijing, 100191, China*
[5.] *Key Laboratory of Fluid and Power Machinery, Xihua University, Chengdu, 610039, China*

ABSTRACT

The aerodynamic performance of axial compressor rotors is negatively affected by the ingestion of boundary layer fluids upstream. As the boundary layer becomes thicker, the blade tip load increases and the local loss is aggravated, especially under off-design operating conditions. The major objective of this research is to evaluate the potential for novel blade sweep designs that can tolerate the ingested low-momentum boundary layer fluids. An optimization design approach using a surrogate model and genetic algorithm is employed. By altering the blade stacking line, the optimized sweep design is obtained. The flow mechanisms that enable the performance of the compressor rotor to be improved are fully analyzed, and the findings indicate that the aerodynamic advantages primarily stem from two key aspects. First, in the tip region, the blade loads are decreased at various chordwise locations and the interaction of the tip leakage flow with the mainstream is alleviated. As a result, the loss near the tip is reduced. Second, the blade sweep design alters the distribution of shock intensity across the spanwise direction, leading to a decrease in shock wave intensity in the mid-span region. This is beneficial in reducing the shock wave/boundary layer interaction strength at the trailing edge of the blade airfoil. Overall, after the sweep design has been optimized to ingest the upstream boundary layer, the compressor rotor experiences a 0.8% improvement in adiabatic efficiency compared with the baseline rotor, while preserving the total pressure ratio and stall margin. Additionally, the redesigned compressor retains the overall performance level under clean inlet conditions. This research provides a potentially effective blade sweep optimization design strategy that allows transonic compressor rotors to tolerate low-momentum upstream boundary layer incoming flows.

Article History

Received April 8, 2024
Revised June 11, 2024
Accepted June 19, 2024
Available online October 2, 2024

Keywords:

Blade sweep
Transonic compressor rotor
Aerodynamic loss
Upstream boundary layer ingestion
Optimization design

1. INTRODUCTION

Transonic axial-flow compressor rotors are key components in compression systems, and are widely applied in aero-engines. Their aerodynamic characteristics play a crucial role in shaping the overall performance of aircraft. Compressors suffer various flow losses, including the shock loss, endwall loss, mixing loss, and tip leakage loss (Denton, 1993). Over recent decades, numerous studies have attempted to reduce the aerodynamic losses in compressor with nearly clean and uniform axial velocity profile conditions (Ma & Li, 2008; Li et al., 2018; Hu et al., 2019). However, the endwall boundary layers cannot be neglected in the presence of large-scale turbulence and crosswinds, under various flight actions such as pitching and rolling, and when flight configurations trigger distorted inflows (Gil-Prieto et al., 2019; Castillo Pardo & Hall, 2021). Therefore, exploring efficient ways to avoid poor aerodynamic performance when the upstream endwall boundary layer fluids are fully considered is of great significance.

The upstream endwall boundary layer fluids distort the inflow working condition at the inlet of a compressor. The inflow distortions can be divided into the total temperature distortion, total pressure distortion, swirl distortion, and combinational

distortion. Based on the spatial distribution of the distorted region, the inlet distortion can be categorized as radial distortion, circumferential distortion, or combinational distortion (Li et al., 2022). The radial total pressure distortion generally originates from an increment in the upstream low-momentum boundary layer thickness (Li et al., 2020), resulting in a high-incidence-angle incoming flow that pushes the local region of the compressor blade into off-design conditions. In such situations, the flow loss near blade tip region is severely aggravated. The impacts of upstream boundary layer fluids near the compressor casing on aerodynamic performance have been extensively investigated in previous research (Wagner et al., 1985a, b; Brossman et al., 2014).

Hunter & Cumpsty (1982) found that the adiabatic efficiency and stall margin of axial-flow compressors are significantly influenced by the low-momentum boundary layer development near the endwall. Further, Brandt et al. (2002) studied a compressor rotor and demonstrated that an increase in the inflow boundary layer (IBL) thickness causes tip leakage vortex to roll up towards blade leading edge. This phenomenon can lead to additional aerodynamic losses within the endwall area. Zhang et al. (2014) explored the impact of the IBL thickness on rotor performance and found that, under design conditions, augmenting the thickness of the IBL in the tip area prompts a forward shift in both the initial position of the tip leakage vortex and the interface of the interaction between the mainstream and leakage flow. This leads to a decrease in both compressor's adiabatic efficiency and total pressure ratio. In addition, as the compressor approaches the stall conditions, the flow blockages and losses increase violently, diminishing the stable operating range. According to the above results, it can be inferred that a thick boundary layer inflow results in the diminished aerodynamic performance of compressors due to the presence of low-momentum fluids in blade tip region.

In recent years, several design techniques for compressors have been explored in an attempt to alleviate the negative effects of low-momentum boundary layer fluid near blade tip region. Li et al. (2017) developed a stall precursor-suppressed casing treatment that bolsters the stall margin under tip radial distortion conditions. Li et al. (2020) investigated the effectiveness of tip air injection in improving the stall margin of a multistage compressor in the presence of tip radial distortion. Although these design techniques offer insights into how future compressor designs could ameliorate the impact of upstream boundary layer inflow conditions, they primarily focus on enhancing the compressor's stable operating range. As a result, effective design approaches for reducing the aerodynamic loss and improving the efficiency of compressors remain relatively scarce. The development of more efficient design strategies could provide dependable technical support for future high-performance compressor designs.

To improve the compressor efficiency under thick upstream boundary layer ingestion conditions, novel blade sweep designs are required. Blade sweep designs can be categorized into forward sweep and backward sweep. In the case of forward sweep, the stacking line is swept in the upstream direction towards the endwall; backward sweep shifts the stacking line in the opposite direction (Sasaki & Breugelmans, 1998). Gümmer et al. (2001) conducted simulations of a subsonic fan to study the working mechanism of blade sweep. Their results show that the sweep design can alter the radial load distribution by transporting low-momentum fluids radially. Hah et al. (1998) investigated the effect of blade sweep on a transonic compressor rotor through numerical simulations, and demonstrated that the sweep design could alter the shock wave structure, consequently changing the shock wave/boundary layer interaction intensity. Furthermore, different blade sweep design schemes have been studied to provide guidelines for actual engineering applications, including forward (Passrucker et al., 2003; Bergner et al., 2005; Sun et al., 2019) and backward (Blaha et al., 2000; Govardhan et al., 2007; Huang et al., 2020) sweep designs and hybrid configurations (Zheng et al., 2010; Okui et al., 2013). An effective blade sweep design can redistribute the radial blade load to improve the compressor efficiency, indicating its potential utility in reducing high blade tip loads under IBL conditions.

In this paper, we describe how the aerodynamic losses under upstream boundary layer ingestion conditions can be suppressed using a blade sweep design strategy for a transonic compressor rotor that is well-designed. The significance of the work is its potential to mitigate the negative effects of upstream low-momentum incoming flow conditions. First, the thickness of the upstream boundary layer is considered. Next, an optimization design approach (Song et al., 2014; Khalfallah et al., 2015; Lu et al., 2018) has been utilized to obtain the optimal blade sweep design. The potential effects on the compressor's aerodynamic performance are subsequently assessed. Finally, the internal flow field is analyzed to gain insights into the influences of blade sweep design on the aerodynamic loss.

2. TRANSONIC COMPRESSOR ROTOR

In this study, NASA's Rotor 67 serves as the baseline design; this is a high-performance and well-documented transonic axial-flow compressor. The geometry of the studied compressor is presented in Fig. 1. The rotor comprises 22 multiple-circular-arc blades. The hub-to-tip ratios at the inlet and outlet are 0.375 and 0.478, respectively. The blade solidities at the hub and tip are 3.11 and 1.29, respectively. Under the design working condition, the rotation speed of the rotor is 16043 rpm, a mass flow rate of 33.25 kg/s is maintained, resulting in a total pressure ratio of 1.63. Table 1 presents additional essential aerodynamic and geometrical parameters. For a more detailed introduction to the compressor rotor, please refer to the listed reference (Strazisar et al., 1989).

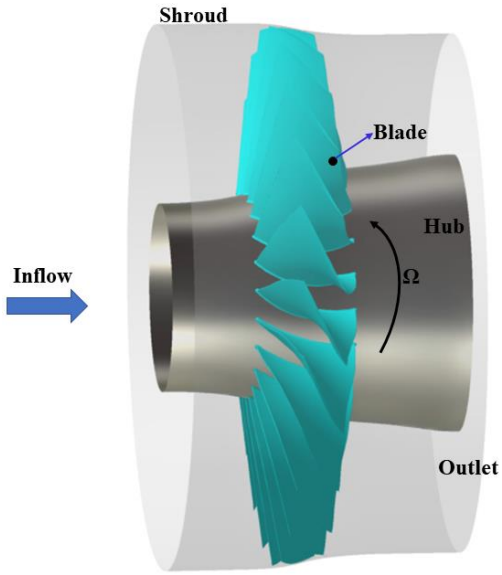

Fig. 1 Graphical representation of the researched compressor rotor

Table 1 Design parameters of the compressor rotor

Blade parameters	Value
Inlet tip relative Ma	1.38
Tip speed (m/s)	429
Aspect ratio	1.56
Tip clearance size (m)	0.001
Load coefficient ($\psi=\Delta h_t/U^2_{mid}$)	0.56

3. COMPUTATIONAL TECHNIQUES

3.1 Computational Methods

The NUMECA FINE-Turbo EURANUS flow solver is selected for its ability to handle the three-dimensional compressible Reynolds-averaged Navier–Stokes equations based on a finite volume approach. Spatial discretization is achieved using a central difference scheme with second-order precision, while temporal discretization utilizes the fourth-order Runge–Kutta technique. The working fluid is assumed to be ideal air. To model turbulence, the Spalart–Allmaras turbulence model (He et al., 2021; Wang et al., 2023) is employed. Additionally, the multigrid technique is utilized to expedite numerical convergence and guarantee a converged solution for the flow field.

Along the annulus, periodic boundary conditions are applied within the computational domain, which encompasses a single blade passage. The inlet is positioned approximately 1.5 times the axial chord length upstream of the leading edge, meanwhile approximately twice the axial chord length downstream of the trailing edge, the outlet is positioned. The inlet is assigned specific conditions for the axial inflow, total pressure and total temperature, whereas the outlet is defined by the prescribed averaged static pressure. All solid walls have been subject to isentropic and no-slip boundary conditions.

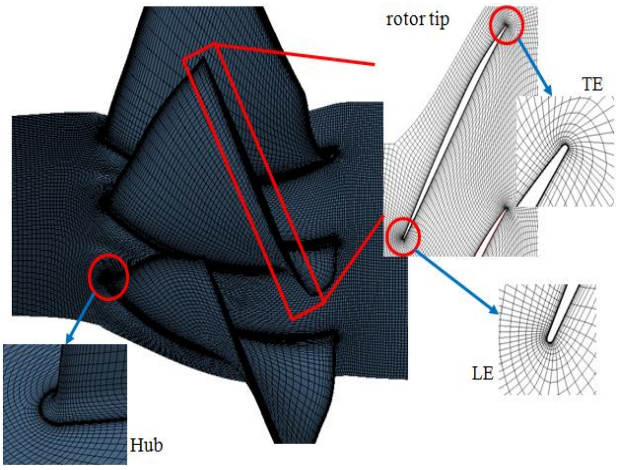

Fig. 2 Computational mesh of the compressor rotor

A multi-block O4H-type structured grid setting has been used for the computational domain; the exception is the rotor tip clearance region, where a butterfly mesh is employed. Specifically, the blade is encircled by an O-type grid, and the H-type mesh is used in other zones. Prior research has demonstrated that a radial distribution of 17 mesh points within rotor clearance zone provides accurate predictions of the clearance flow fields (Zhang et al., 2014). Consistent with these findings, this study employs a mesh that incorporates 17 grid points to precisely simulate the local flow in the tip clearance zone. Figure 2 presents the grid for the computational domain of compressor rotor. For every simulation case, the y+ value is consistently less than 5 in proximity to solid walls. In efforts to eliminate potential effect of mesh topology on the results, both baseline and modified blade designs employ the same mesh template to create the computational mesh.

To evaluate the impact of grid size on the simulation results, a grid-independence study is undertaken. Three distinct mesh sizes, namely Grid A, Grid B, and Grid C, are chosen for numerical simulations. These simulations are conducted using identical boundary conditions. Figure 3(a) shows two vital performance parameters given by the three meshes: the total pressure ratio and adiabatic efficiency. In the case of the adiabatic efficiency, transitioning from Grid A to Grid B produces a 2.57% variation, notably larger compared with the 0.49% variation observed when moving from Grid B to Grid C. In terms of the total pressure ratio, a shift from Grid A to Grid B leads to a 0.24% variation, exceeding the 0.19% variation seen in the transition from Grid B to Grid C. Comparisons of rotor efficiency at different span locations using the three mesh sizes are illustrated in Fig. 3(b). For Grid B, the computed efficiency values are closely aligned with those for Grid C across the entire blade height. However, Grid A produces significant deviations from the results for Grids B and C, particularly from 0%–80% span. To ensure computational accuracy at a reasonable computational spent, for all subsequent numerical simulations, Grid B is employed.

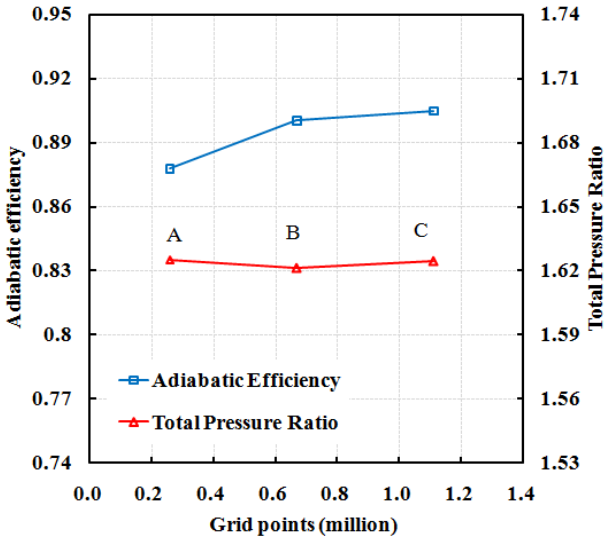

(a) Variations of aerodynamic performance parameters

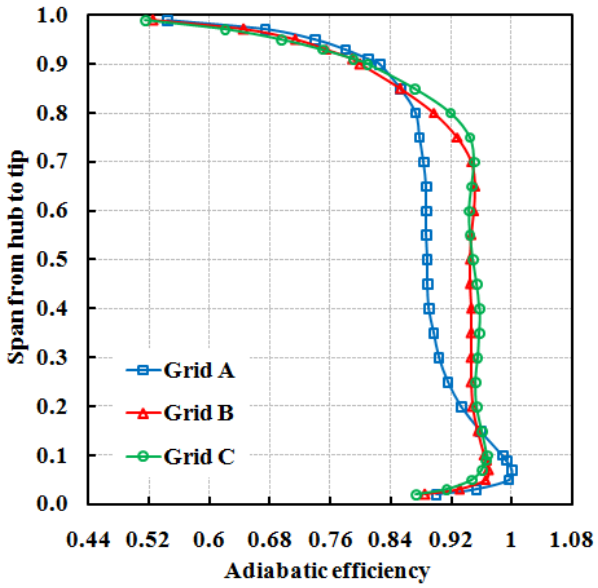

(b) Adiabatic efficiency along the radial direction

Fig. 3 Results of grid independence study

Throughout this research, the convergence of every simulation is ensured by maintaining the variations in the mass flow rate at both the inlet and outlet below 10^{-5} across the final 50 iterations. Solutions generally converge within approximately 1000 iterations, aided by setting appropriate initial values. However, under low mass flow rates, additional iterations may be required to achieve convergence. The discrepancy in the mass flow rate at the inlet and outlet is maintained at less than 0.02%.

3.2 CFD Validations

To enhance the credibility of the numerical approach, this study conducts comparative analysis between the experimental results (Strazisar et al., 1989) and CFD results. These comparisons focus on two elements: the compressor performance maps and the specific flow fields.

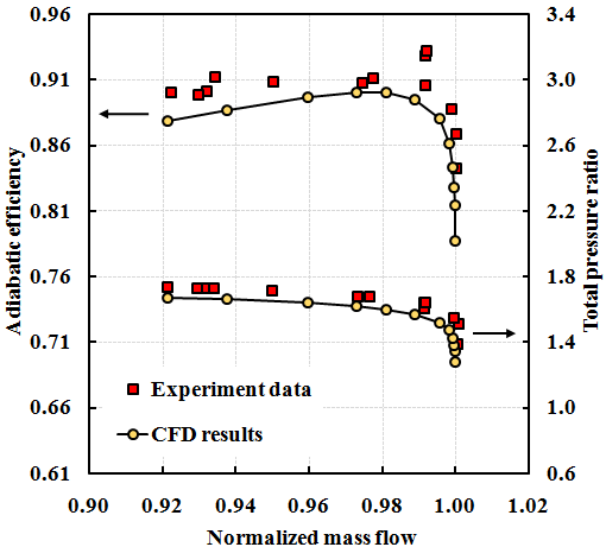

Fig. 4 Comparison of performance maps

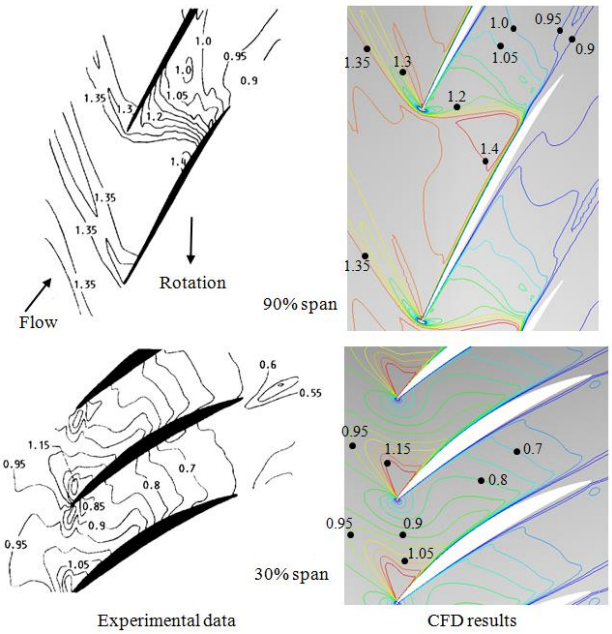

Fig. 5 Comparison of relative Mach number distributions at near peak efficiency condition

Figure 4 compares the performance curves under clean inflow conditions. The adiabatic efficiency, as estimated through the CFD approach, aligns closely with the experimental data, albeit with slightly lower magnitudes. Furthermore, the total pressure ratio given through CFD simulations exhibits good consistency with the experimental data. Although there are some minor deviations in absolute values, the CFD tool successfully predicts the trends in performance.

Figure 5 compares the relative Mach number contours under near-peak-efficiency conditions at 30% and 90% blade spans, showcasing the numerical tool's effectiveness in capturing flow-field details. The 30% and 90% spans are selected because they represent the flow structures in transonic and subsonic regimes, separately. For 90% spanwise fraction, the positioning

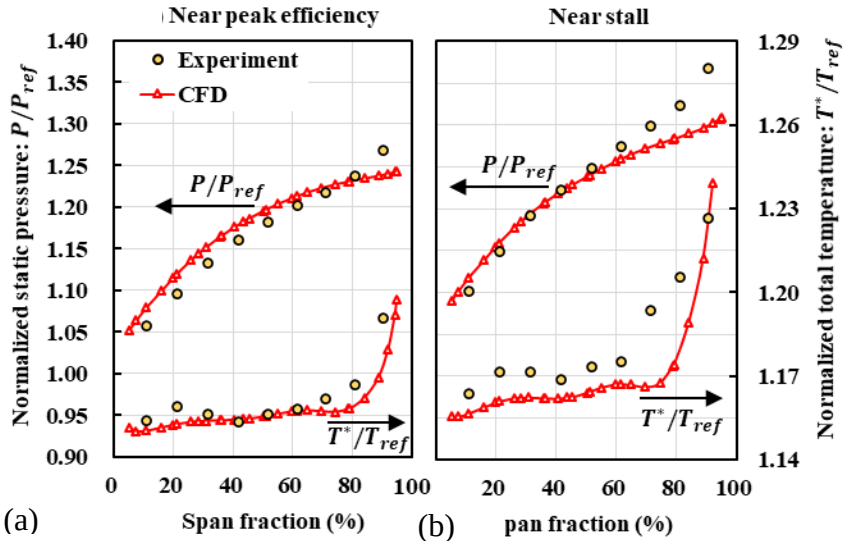

Fig. 6 Comparisons between the aerodynamic parameter distributions along the radial direction from CFD simulations and experimental data at near peak efficiency and near stall points.

and strength of shock waves within the blade passage are in excellent agreement with the experimental results, except for a slightly larger predicted region of high relative Mach numbers near the suction surface. At 30% spanwise fraction, the CFD results align well with the experimental data, although the relative Mach number near the blade leading edge transitions more rapidly from high-Ma isolines to low-Ma isolines.

At the near-peak-efficiency point and near-stall point, Fig. 6 illustrates a comparison between the radial distributions of total temperature and static pressure. The CFD tool accurately captures the variations in the total temperature and static pressure at different span fractions under both operating conditions.

Considering the validation results outlined above, it is concluded that the CFD tool applied in this research reliably and accurately predict the performance curves and flow-field details for a transonic compressor rotor.

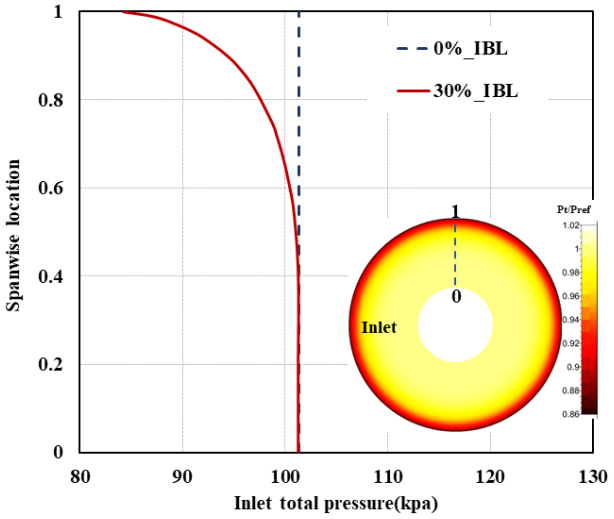

Fig. 7 Profiles of the inlet boundary layer conditions

4. PROBLEM DESCRIPTIONS

Generally, axial compressors are optimized for clean inflow conditions. In recent years, significant advances have been made in enhancing the performance of compressors in the case of a clean inflow. However, during real flying operations, the compressor blades frequently operate under IBL conditions, potentially leading to seriously degraded aerodynamic performance. Specifically, the presence of the endwall low-momentum boundary layer fluid near blade tip area can subject the corresponding blade airfoil sections to high-load off-design conditions. Simultaneously, the spanwise mass flow is redistributed, which changes the operating conditions at other span fractions. In such scenarios, design considerations based solely on clean inflow conditions become unsuitable.

Based on previous results regarding the upstream inlet boundary layer thicknesses (Zhang et al., 2014) and their impacts on rotor performance, a 30% IBL thickness in the tip region is selected to depict the deteriorated inflow conditions. An IBL thickness of 0% is also employed as a comparison. The inflow total pressure profiles under both boundary layer thicknesses are illustrated in Fig. 7. Importantly, this study employs an axisymmetric inlet distortion condition to conduct fundamental research. This condition is even more challenging than real-world applications, such as BLI fans. Specifically, it involves a thick boundary layer along the entire circumference, rather than just along certain sectors. If optimization succeeds under these conditions, it can be naturally extended to real applications and may even yield superior performance.

Figure 8 compares the efficiency performance maps under the 0% and 30% IBL thickness working conditions. The maximum efficiency with the 30% IBL thickness decreases by about 1.4 percentage points compared with that under 0% IBL thickness. Additionally, there is a significant reduction observed in

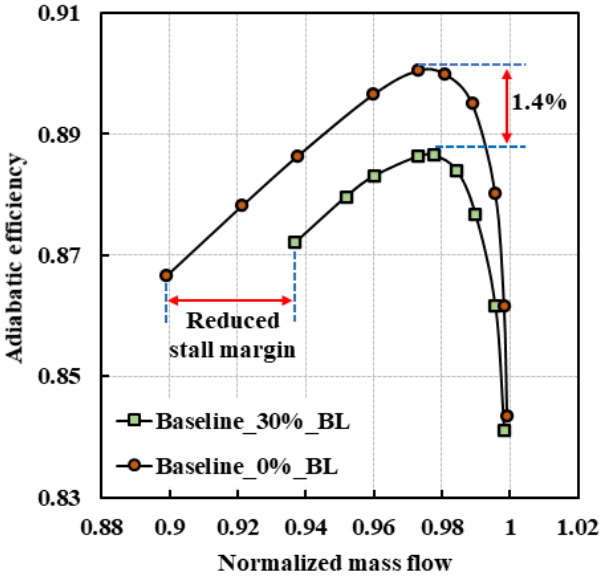

Fig. 8 Rotor performances at 0% and 30% inlet boundary layer thickness conditions

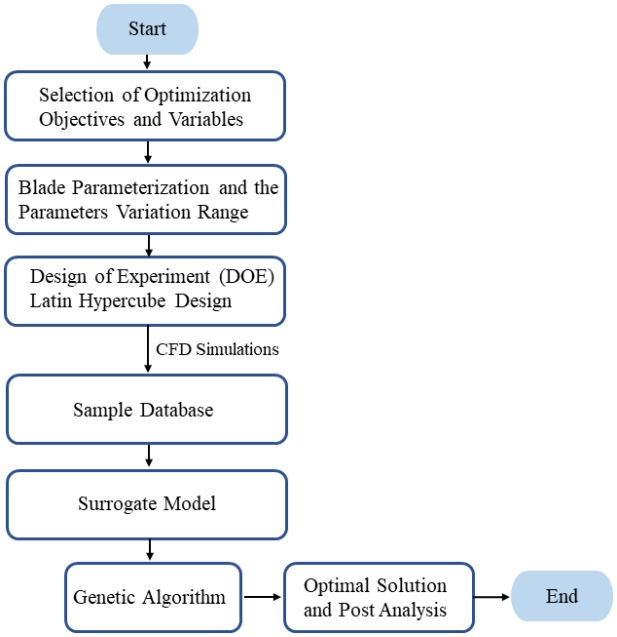

Fig. 9 Flowchart of the optimization procedure

the stable operating range. In such a situation, our motivation is to develop a blade sweep design that enhances the compressor robustness under upstream boundary layer ingestion conditions while at least maintaining the aerodynamic performance under clean inflow conditions. Ideally, the potential design strategy for transonic compressors should have the ability to withstand challenging upstream low-momentum boundary layer ingestion conditions.

5. Optimization Approach

5.1 Optimization Procedure

An integrated optimization procedure encompassing four key elements is implemented: blade parameterization, design based on Latin hypercube sampling, a dependable flow-field solver, and an optimization toolkit. The optimization design process is outlined in Fig. 9. Initially, the geometric parameters influencing compressor aerodynamic performance are identified as design variables. Subsequently, the blade geometry undergoes a parameterization process, and the range of variation for these design variables is confirmed according to the actual geometrical constraints and specific problem features. The experimental design methodology (Latin hypercube design) is used to create a distribution of sample points. An effective surrogate model is then employed to delineate the relationship between the design variables and the optimization objectives. Ultimately, utilizing an optimization search technique, the surrogate model's response surface is explored to identify the optimal solution.

This study aims to explore the potential of various blade sweep designs to reduce the flow losses under IBL thickness conditions. Achieving these designs requires meticulous blade parameterization. To parameterize the airfoil sections of blades, mainly the camber line and thickness distribution, eight-parameter Bezier curves are

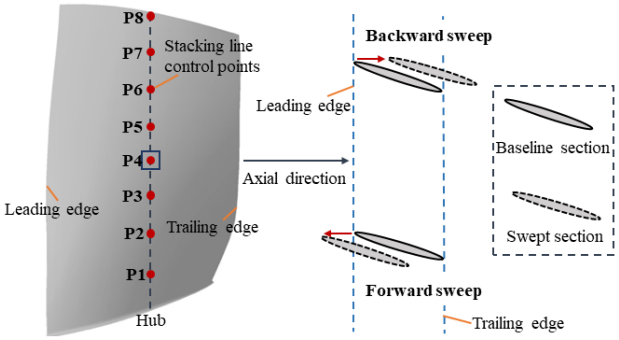

Fig. 10 Diagram of blade sweep definition

utilized. This method is also used to parameterize the blade stacking line. Bezier curves ensure smooth and continuous changes in the objective curves. In the present study, eight control points (P1–P8) are evenly spaced along the stacking line, and the line could be reshaped through adjusting the locations of these points. Consequently, sweep design is realized by shifting these control points in the axial direction (Fig. 10) while keeping the stacking line at the hub end stationary. As the distorted inflows are mainly concentrated in the blade tip region, only four control points (P5–P8) are used to implement the sweep design in this work. Note that the sweep design utilized in this paper is axial sweep (Scott McNulty et al., 2004; Benini & Biollo, 2007). The sweep design process naturally introduces blade lean. Moreover, for each stacking line shape, a sample point is acquired.

5.2 Surrogate Model

This research utilizes an effective surrogate model to establish the correlations between the design variables and the optimization objectives. In order to build this surrogate model, Latin hypercube sampling has been utilized, with an even distribution of sampling points across the design space. The CFD solver provides rotor

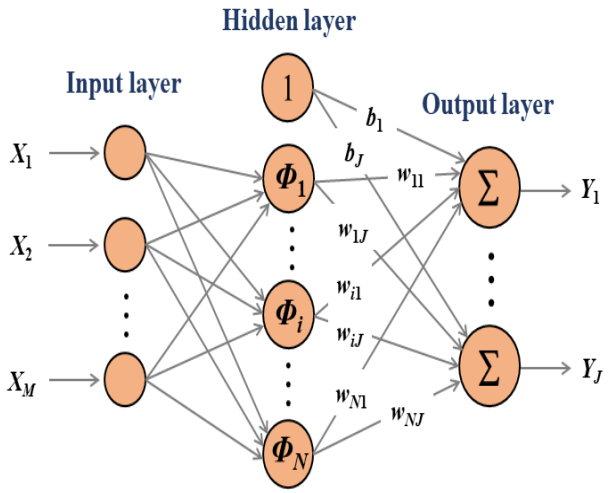

Fig. 11 The architecture of RBF neural network

aerodynamic performance outputs for the generated sampling points. A total of 30 samples are acquired.

The surrogate model employs the radial basis function (RBF). Figure 11 depicts the architecture of the RBF neural network, consisting of an input layer, hidden layer, and output layer.

In the input layer, M represents the dimension of the input vector $\vec{X}_k = [X_1, X_2, \cdots, X_M]$, where k signifies the *k-th* input vector. In the hidden layer, N denotes the node number. In the output layer, J represents the dimensions of output vector $\vec{Y}_J = [Y_1, Y_2, \cdots, Y_J]$.

The RBF neural network operates as follows: initially, the *k-th* input vector undergoes a nonlinear transformation by the Gaussian function Φ_i in the hidden layer. Subsequently, Φ_i undergoes a linear transformation using the weights w_{ij} and bias b_j. Ultimately, the output vector Y_J^k is shown as:

$$\mathrm{Y_J^k} = \sum_{\mathrm{i=1}}^{\mathrm{N}} \mathrm{w_{ij}} \Phi(\vec{\mathrm{X}}^{\mathrm{k}}, \mathrm{C_i}) + \mathrm{b_j}, (\mathrm{k=1:\ K, j=1:\ J}) \tag{1}$$

$$\Phi(\vec{\mathrm{X}}^{\mathrm{k}}, \mathrm{C_i}) = \exp(-\frac{1}{2\sigma^2} \mathrm{P} \vec{\mathrm{X}}^{\mathrm{k}} - \mathrm{C_i\ P^2}) \tag{2}$$

where $\|\cdot\|$ represents the Euclidean norm, σ is the standard deviation of Gaussian function, and C_i (where i ranges from 1 to N) serves as the center of the Gaussian function. The above expression could be expressed more clearly in matrix form:

$$\begin{bmatrix} \vec{Y}^1 \\ \vec{Y}^2 \\ M \\ \vec{Y}^k \end{bmatrix} = \begin{bmatrix} 1 & \Phi(\vec{X}^1, C_1) & \Phi(\vec{X}^1, C_2) & L & \Phi(\vec{X}^1, C_N) \\ 1 & \Phi(\vec{X}^2, C_1) & \Phi(\vec{X}^2, C_2) & L & \Phi(\vec{X}^2, C_N) \\ M & M & M & O & M \\ 1 & \Phi(\vec{X}^k, C_1) & \Phi(\vec{X}^k, C_2) & L & \Phi(\vec{X}^k, C_N) \end{bmatrix} \cdot \begin{bmatrix} b_1 & b_2 & L & b_J \\ w_{11} & w_{12} & L & w_{1J} \\ M & M & O & M \\ w_{N1} & w_{N2} & L & w_{NJ} \end{bmatrix} \tag{3}$$

Equation (3) can be further expressed as:

$$\mathrm{Y = G \cdot BW} \tag{4}$$

The three unknown parameters, namely, the standard deviation σ, the center of the Gaussian function C_i, and the weights and bias (BW), are determined through training with sample data.

Employing the K-means technique, the center of the Gaussian function is determined. Step1: the sample data is randomly selected from the database and set as the initial centers. Step2: the training samples are randomly drawn from the database and set as the input vector. Step3: Calculate the Euclidean distances between centers and input vectors, then assign the training samples to the nearest clusters based on their proximity to these centers. Step4: Recalculate the averaged vectors in each cluster to establish the new centers. Following numerous iterations, when the differences between the new and old centers drop below a certain threshold, convergence is achieved. The final mean vectors are then used to construct the Gaussian kernels:

$$\sigma_i = \lambda \min_{j=1\sim N} \left\| C_i - C_j \right\|, (i = 1 \sim N) \tag{5}$$

The optimization process utilizes an RBF surrogate model, followed by the implementation of a genetic algorithm within MATLAB. The setup for the genetic algorithm includes the population size and a generation count, both set as 100, along with the crossover probability (set as 0.9) and the mutation probability (set as 0.01). The rank fitness scaling strategy is employed. The optimization process continues until the predefined maximum number of generations has been reached.

5.3 Mathematical Model

To maximize the efficiency of the compressor rotor, the optimization design prioritizes the maximum efficiency point, emphasizing the performance enhancement under the IBL operating conditions, meanwhile keeping the compressor's performance under clean inlet conditions. In this scenario, both the clean inlet condition and 30% IBL condition have been considered.

The optimization design problem consists of three fundamental elements: objectives, design variables, and constraints:

Objectives

Under the 30% IBL operating condition, the aim is to attain the highest possible adiabatic efficiency.

$$Max\ \eta_{30\%IBL} \tag{6}$$

where η signifies the isentropic efficiency.

Design variables

Guided by the stacking line, eight control points are utilized during the parameterization stage to characterize the blade sweep. The axial displacement offsets of the four control points nearest the blade tip are identified as the design variables. Thus, the optimization design process incorporates four geometric design variables.

Constraints

The optimization problem is framed by constraints related to both geometry and performance (Li et al., 2024).

Geometric constraints:

1) Maintain a consistent size for the rotor tip clearance.
2) Keep the shroud and hub profiles unchanged.
3) Ensure the sectional airfoils at every spanwise position are unmodified.
4) Preserve the radii of the trailing and leading edges without alteration.

Performance limits:

1) Under the 30% IBL operating condition, to ensure the total pressure ratio is maintained, the following equation must be satisfied:

$$\frac{\left|\pi_{opt\_30\%IBL}-\pi_{base\_30\%IBL}\right|}{\pi_{base\_30\%IBL}}\le\varepsilon \tag{7}$$

where π_{base} and π_{opt} denote total pressure ratio for baseline and optimized designs, respectively, and ε signifies a small fixed value.

2) Ensuring the isentropic efficiency remains constant under the clean inlet condition, it is necessary to employ the following equation:

$$\frac{\left|\eta_{opt\_0\%IBL}-\eta_{base\_0\%IBL}\right|}{\eta_{base\_0\%IBL}}\le\varepsilon \tag{8}$$

3) In order to keep the total pressure ratio under clean inlet condition, the implementation of the following equation is required:

$$\frac{\left|\pi_{opt\_0\%IBL}-\pi_{base\_0\%IBL}\right|}{\pi_{base\_0\%IBL}}\le\varepsilon \tag{9}$$

The mathematical framework for the present optimization problem, drawing from the above expressions, is outlined as follows:

$$\begin{cases}\text{Maximize } \eta_{30\%IBL}\ (x_1,...,x_4)\\ -1\le x_i\le 1\ \ (i=1,...,4)\\ \text{subject to}\\ \text{Eqs. (7)-(9)}\\ \text{and}\\ \text{the geometrical constraints.}\end{cases} \tag{10}$$

where x represents the axial displacement of the control points. The axial displacements are standardized.

6 RESULTS

6.1 Sweep Optimization Design Results

A comparison of blade geometries reveals several distinctions between the baseline and optimal designs (Fig. 12). Notably, the optimized rotor has a backward sweep from the 60% span to the tip region, and features a noticeable forward sweep from the mid-span to the 60% span. Overall, the optimized rotor's stacking line exhibits a slight S-shape from the mid-span to the blade tip.

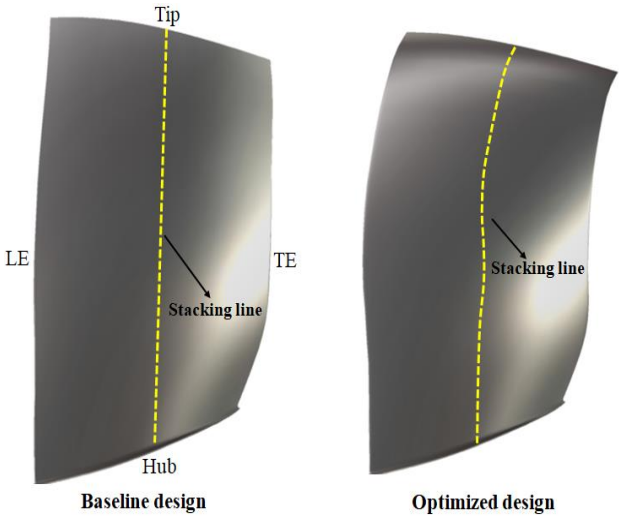

Fig. 12 Comparison of blade geometry in the meridional plane

6.2 Performance Comparisons

Figure 13 presents the rotor performance curves between baseline and modified blade sweep designs under the 30% IBL operating condition. Figure 13(a) shows that blade sweep optimization leads to a notable increase in the rotor's adiabatic efficiency across the whole operating range, with the maximum efficiency of the rotor improving by roughly 0.8%. In addition to the enhanced efficiency, Fig. 13(b) indicates an overall increase in the total pressure ratio across the operating range in comparison with the baseline design. Moreover, the stall margin of the compressor has been enhanced. These results demonstrate that the blade sweep design can significantly improve the compressor aerodynamic performance under IBL working conditions. Furthermore, the results prove that blade sweep design has the potential to deal with the problems introduced by upstream low-momentum IBL ingestion conditions.

To further confirm the potential of the optimized blade sweep design strategy, the rotor performance maps are compared under uniform inflow conditions in Fig. 14. The adiabatic efficiency of the optimal design is slight better than that of the baseline design under low-mass-flow operating conditions. Simultaneously, at large-mass-flow operating conditions, the performance curves are almost the same. For the baseline design and the sweep design, the total pressure ratio maps align closely, suggesting minimal alteration in total pressure ratio with blade sweep optimization under uniform inflow conditions. Furthermore, a slight increase in the stable operating range of the rotor is observed when compared to the baseline design.

Figure 15 illustrates the efficiency improvement at different spanwise locations. The efficiency improvement is defined as the deviation of the efficiency from the optimized design to the baseline design. With the optimized blade design, the efficiency improves at almost all spanwise locations, with the exception of a slight decrease at around 85% spanwise location. Along the full

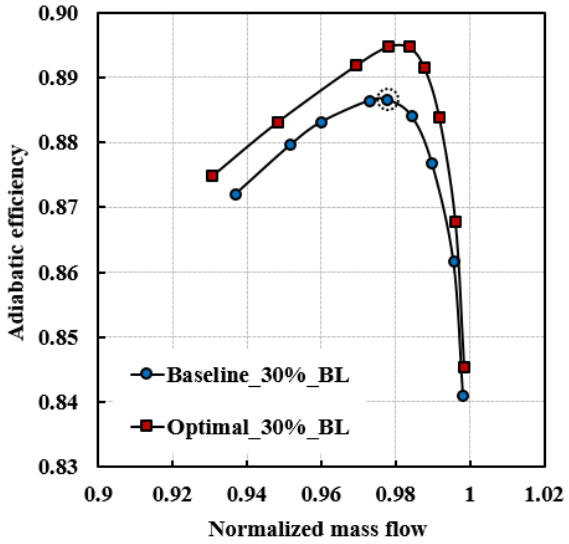

(a) Adiabatic efficiency characteristic

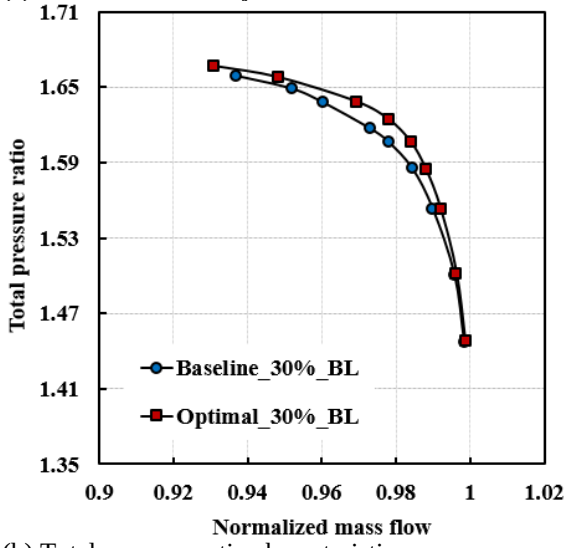

(b) Total pressure ratio characteristic

Fig. 13 Comparisons of performance maps under 30% IBL operating condition

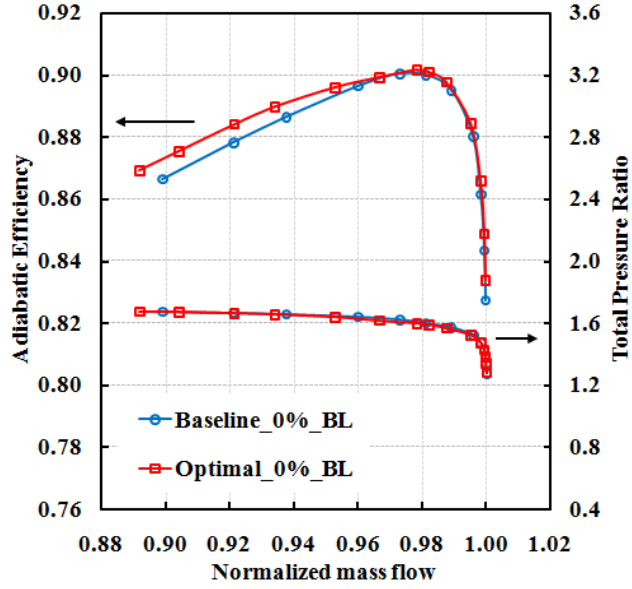

Fig. 14 Comparisons of rotor performance maps under uniform inflow condition

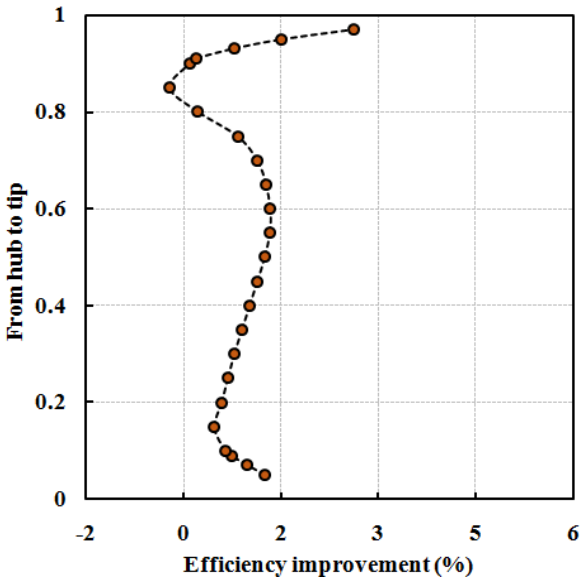

Fig. 15 Efficiency improvement relative to the baseline design at different spanwise locations at the maximum efficiency point

span, the blade tip region achieves the greatest aerodynamic benefit, mainly at spanwise locations above 90% span and the mid-span regions from 40%–70% span. To explore the loss reduction mechanisms in these two spanwise regions, the specific impacts of the optimized sweep design on the flow field under IBL conditions are now analyzed.

6.3 Effects on Clearance Leakage Flow

To examine the loss distributions within clearance region, Fig. 16 contrasts the entropy loss coefficient distributions within the blade tip clearance at maximum efficiency point. The entropy loss coefficient is defined as:

$$\zeta = \frac{T_1 \Delta s}{0.5 \cdot V_1^2} \tag{11}$$

where Δs represents alteration in entropy flux across the rotor blade, and T_1 and V_1 signify static temperature and inlet velocity, respectively.

The entropy loss contours are derived from cross planes at different chordwise locations. The 12% and 73% chord length locations are chosen because they reflect the loss before and after the shock, respectively. Figure 16(a) indicates that, at the 12% chord length location, the high-entropy region inside the tip clearance is significantly reduced by the optimized sweep design compared with the baseline rotor. Figure 16(b) shows that the high-loss region inside the tip clearance is reduced at the 73% chord length location, but the loss reduction magnitude is much smaller than that at 12% chord length. These results demonstrate that sweep optimization has positive effects on controlling clearance leakage flow.

To analyze the significant loss reduction within the tip clearance at the 12% chordwise location, the relative kinetic energy contours on the cross-plane at 12% chord

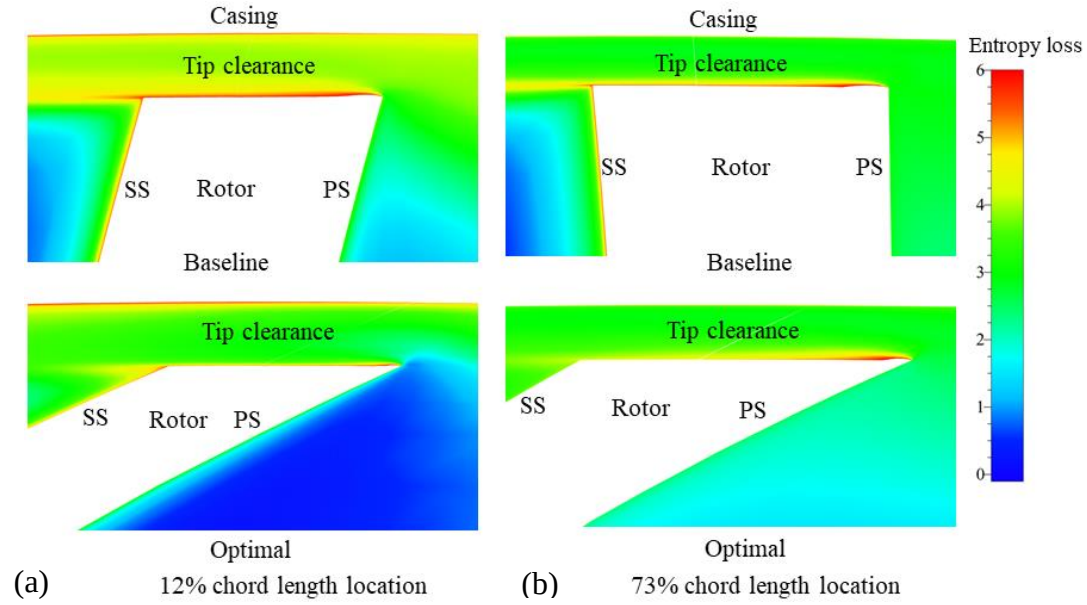

Fig. 16 Comparisons of entropy loss distribution on the cross planes at different chordwise locations inside the tip clearance

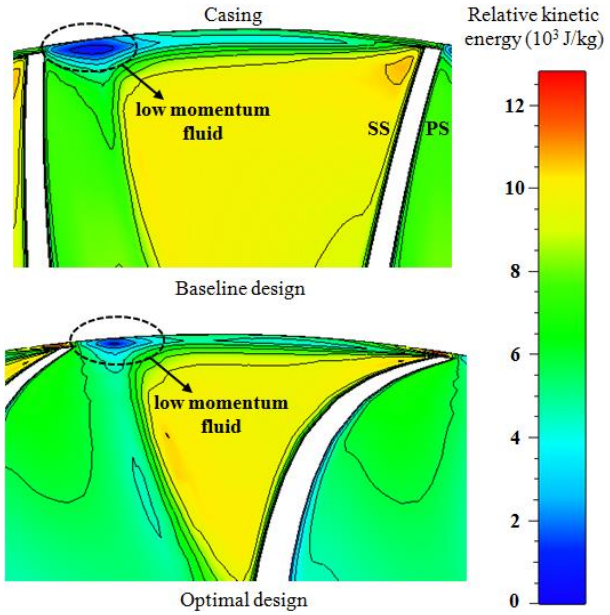

Fig. 17 Comparisons of relative kinetic energy contours on the cross plane at 12% chordwise location

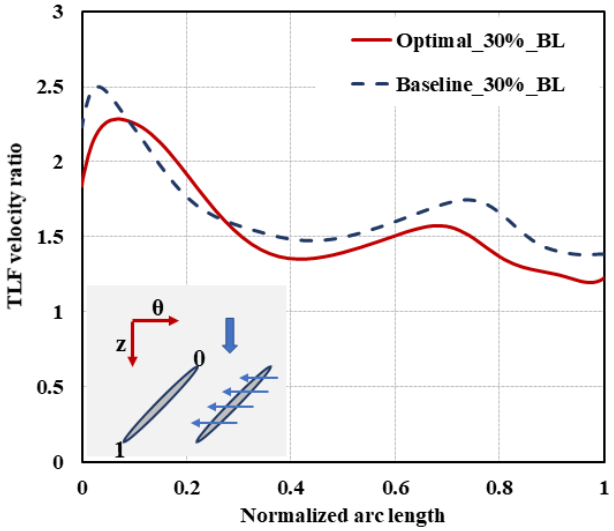

Fig. 18 Comparison of velocity ratio distributions along the chordwise direction between the optimized sweep design and the baseline design

length are presented in Fig. 17. There is a notable area of low-momentum fluid near the casing endwall. The flow blockages are mainly introduced by the mainstream and tip leakage flow interaction, and are driven towards adjacent blade by the pressure difference across the blade passage. After sweep optimization, the region of low-momentum fluid becomes much smaller than that in the baseline design. The results show that the sweep design is advantageous in suppressing the interaction intensity of mainstream/tip leakage flow, and in reducing flow blockages near the casing endwall.

To further illustrate the variation in the interaction intensity of mainstream/tip leakage flow, Fig. 18 presents the chordwise distribution of the ratio between the axial velocity of the mainstream and the tangential velocity components of the tip leakage flow. This velocity ratio describes the interaction strength of the tip leakage flow and the mainstream, and is defined as:

$$\sigma = W_t / W_z \tag{12}$$

where σ denotes the velocity ratio, W_t represents the averaged tangential velocity of the tip leakage flow at different chordwise locations, and W_z is the mass-averaged axial velocity of the mainstream above 90% span. Larger values of the velocity ratio indicate a stronger interaction.

The interaction of mainstream/tip leakage flow directly results in mixing loss and flow blockage. The

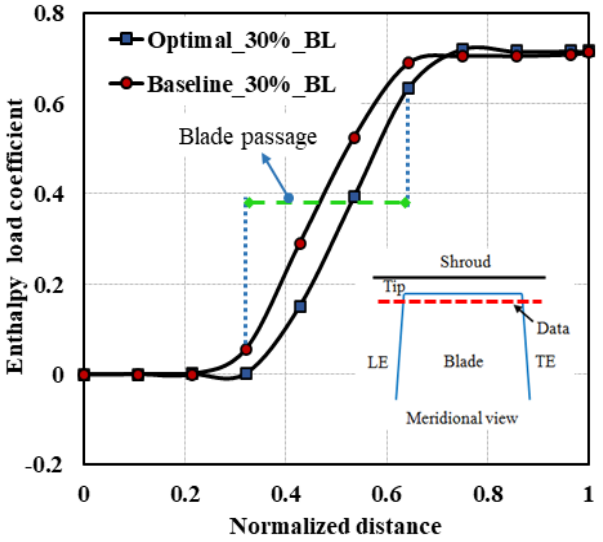

Fig. 19 Comparison of blade load distributions at different chordwise locations at 95% span

velocity ratio in the tip region is smaller under the optimized sweep design than with the baseline design at different chordwise locations (from blade leading edge to trailing edge, or from blade inlet to outlet), except from about 10% chord length to 25% chord length. Specifically, the velocity ratio decreases significantly near the leading edge (from blade leading edge to about 10% chordwise location) and near the trailing edge (from about 75% chordwise location to trailing edge). These results indicate that, the optimized sweep design yields notably diminished tip leakage flow intensity, leading to significantly lower levels of leakage loss and blade load.

Figure 19 compares the blade load distributions at different chordwise positions at 95% spanwise fraction. The load coefficient is defined as follows based on enthalpy:

$$\psi = \Delta h_t / U_{mid}^2 \tag{13}$$

where U_{mid} denotes the blade rotation velocity at midspan and Δh_t is the total enthalpy increment. The total enthalpy increment at different chordwise locations is calculated relative to the enthalpy value of the reference point (normalized distance of zero). The normalized distance is defined as:

$$D_{norm} = (L - L_1) / (L_2 - L_1) \tag{14}$$

where D_{norm} denotes the normalized axial distance, L is the local axial location, L_1 represents the initial axial location, and L_2 signifies the terminal axial location. In comparison with the baseline, the tip backward sweep successfully decreases the blade load from the blade inlet to blade outlet. This reduction decreases the losses inside the tip clearance and reduces the intensity of the tip leakage jet.

The entropy loss contours for blade-to-blade section at 99% span are compared in Fig. 20. The leakage flow leaves the tip clearance near the blade leading edge and interacts with the mainstream. The shear stress causes a large-scale leakage vortex and creates a high-entropy-loss area near the adjacent blade pressure side, which corresponds to the low-momentum fluid region in Fig. 17. The reduction in the local blade load given by the optimized tip backward sweep design decreases the interaction intensity of the mainstream/leakage flow, significantly decreasing maximum loss value. As a result, the flow blockages near the casing are eliminated.

As a quantitative illustration of the loss variation in the tip area, Fig. 21 compares the mass-averaged entropy distribution at different chordwise positions from upstream blade inlet to downstream blade outlet at 95% span. After sweep optimization, the entropy creation is much lower than that for the baseline design at different chordwise locations. These results demonstrate that the tip aerodynamic loss has been fully suppressed because of the decreased blade load and the associated elimination of the tip leakage flow.

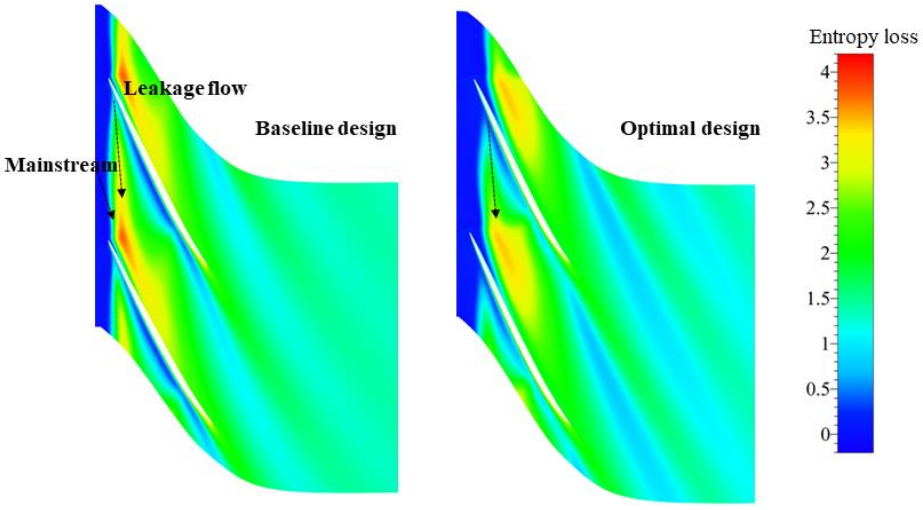

Fig. 20 Comparison of blade-to-blade entropy loss contour at 99% span

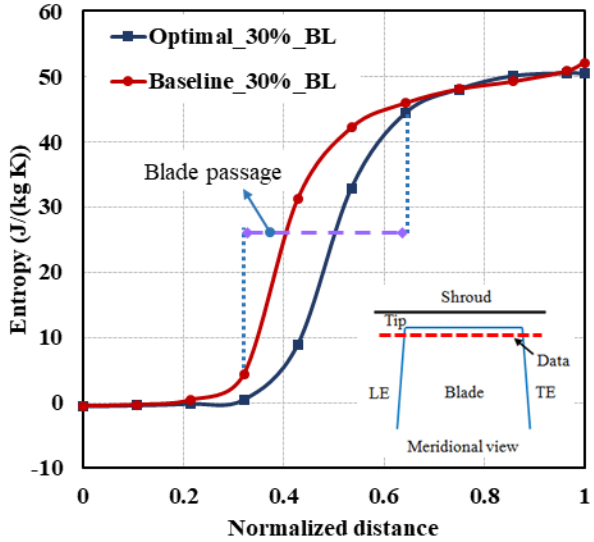

Fig. 21 Comparison of the entropy chordwise distributions at 95% span

6.4 Effects on Flow Structure at Mid-Span

The adiabatic efficiency exhibits a remarkable improvement from 35%–75% span following sweep design optimization. The reasons for the local aerodynamic benefit have been revealed in this section. Across these spanwise fractions, the main aerodynamic loss comes from the interactions between the shock and the local boundary layer fluid. Therefore, it is important to consider variations in shock intensity and the associated boundary layer separation.

The shock plays an important role in the blade load distribution. Figure 22 compares the pressure coefficient contours on the suction side as a means of depicting the shock wave distribution. The definition of pressure coefficient is:

$$Cp = (P_{wall} - P_{in}) / (P_{in}^{*} - P_{in}) \tag{15}$$

where P_{in}^{*} denotes the inflow total pressure, P_{wall} is the static pressure near the blade, and P_{in} signifies the inflow static pressure. Comparisons illustrate that, for the baseline rotor design, the shock (marked by purple dotted box) passes from the blade tip to approximately 25% blade span. However, for the optimized sweep blade design, the shock is confined to the region from the blade tip to around 50% blade span. This implies that the influence range of the shock is mitigated. Moreover, in the mid-span region, the more relaxed distribution of isolines around the shock in the optimized sweep design indicates a reduction in the shock intensity, which suggests that the impact of the shock wave on the local flow field could be mitigated.

From another angle, Fig. 23 shows the pressure coefficient contours on the blade-to-blade surface at 50% span. Observations reveal that, in the optimized sweep design, the pressure coefficient isolines become sparse in the blade passage, reflecting a shallower local adverse pressure gradient. In this situation, the decreased shock intensity is beneficial for reducing the blade load and preventing an accumulation of thick low-momentum boundary layer fluid.

In Figure 24, a comparison is made between the relative Mach number contours encircling blade surface. The low-momentum boundary layer fluid is mainly generated after the shock. As the shock intensity decreases, the interaction of the boundary layer and shock wave is gradually eliminated. As a result, the boundary layer near the blade's trailing edge becomes thinner. Moreover, downstream of the rotor, the wake region becomes smaller, resulting in reduced mixing loss.

Figure 25 illustrates the distribution of entropy loss along the annulus at the outlet of the blade passage, highlighting variations in the wake zone and demonstrating local aerodynamic losses. The findings reveal that, between the 60%–90% annular locations, the optimized blade sweep design yields reduced aerodynamic loss compared to the baseline design. This enhancement is credited to the elimination of the wake area near the trailing edge. This reduction in the loss due to shock wave/boundary layer interaction is beneficial for improving the local blade performance.

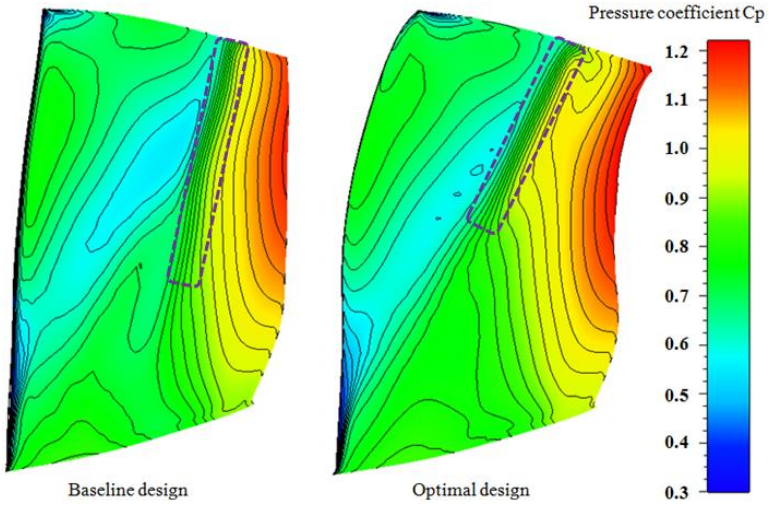

Fig. 22 Static pressure contours for the blade suction side for baseline and optimal designs

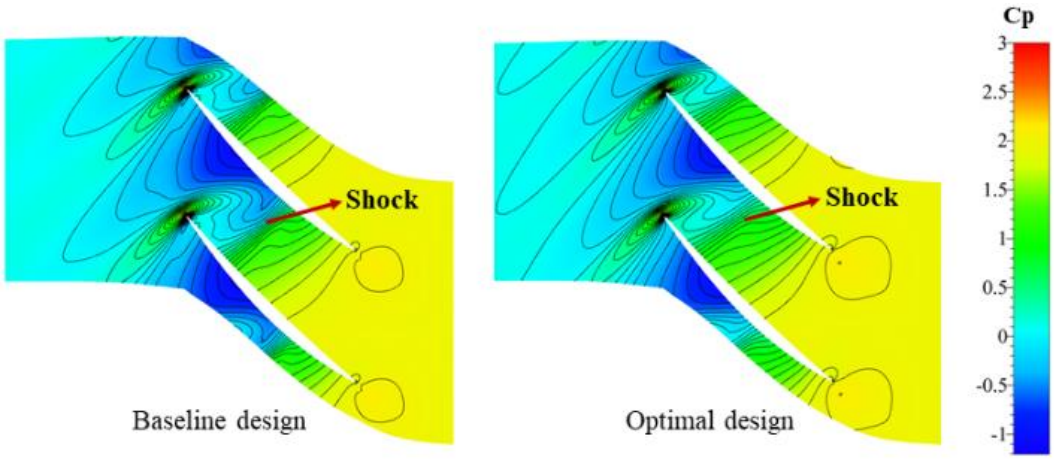

Fig. 23 Blade-to-blade static pressure contours at 50% span for baseline and optimal designs

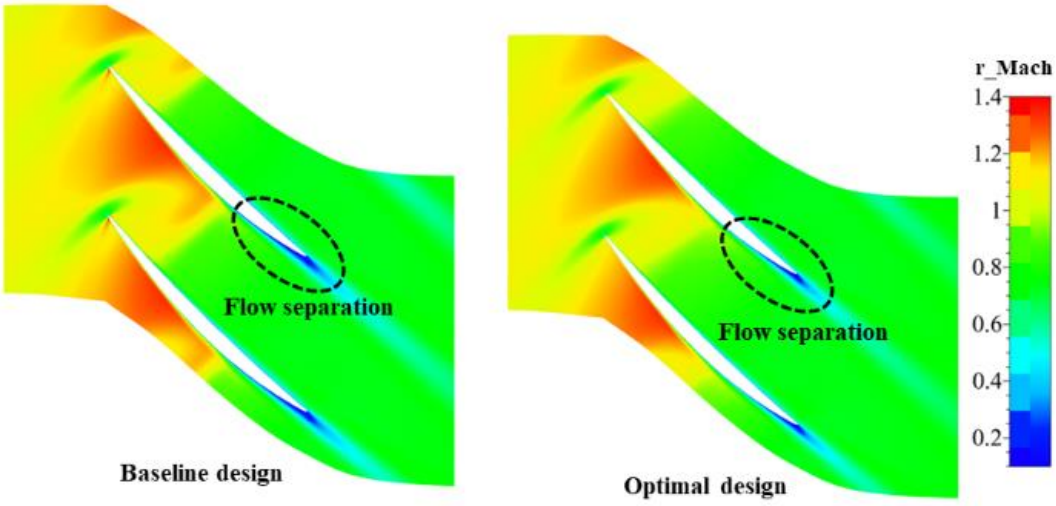

Fig. 24 Blade-to-blade relative Mach number contours at 50% span for baseline and optimal designs

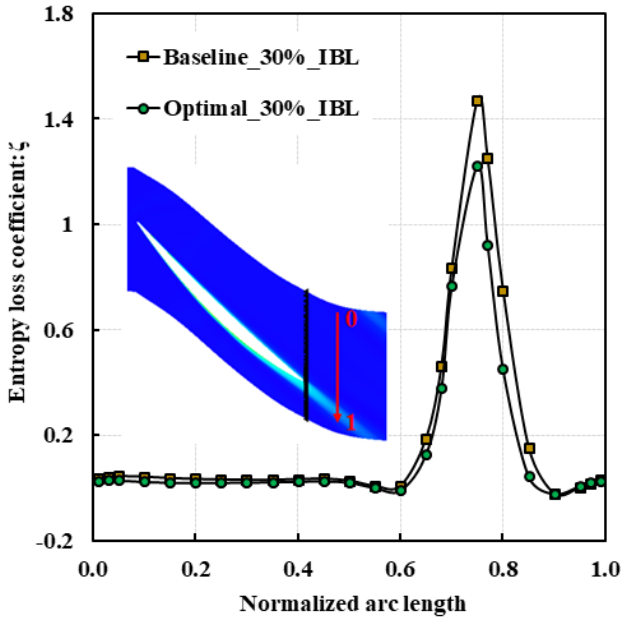

Fig. 25 Entropy loss distributions at different pitchwise locations at the blade passage outlet (50% span)

7 SUMMARY AND CONCLUSIONS

This paper has investigated the potential of blade sweep optimization to enhance the compressor aerodynamic performance under upstream boundary layer ingestion conditions. An optimization design approach was employed, utilizing a surrogate model and a genetic algorithm. By altering the local stacking line, the optimal blade sweep design was obtained, and the main factors contributing to efficiency improvements were analyzed. The following conclusions can be drawn from this study:

(1) Regarding the leakage flow inside the tip clearance, the optimized blade sweep design effectively reduces the losses inside the clearance region, especially at earlier chordwise locations. The optimized sweep design also reduces the leakage flow intensity and the associated interaction intensity between mainstream and leakage flow, which leads to a reduction in flow blockages near the casing endwall. Moreover, the entropy distribution at different chordwise locations for 95% span fraction suggests that the flow losses are reduced in the blade tip area. These findings

highlight that the optimized sweep design is beneficial in decreasing the leakage loss under low-momentum upstream boundary layer ingestion conditions.

(2) The optimized sweep design reorganizes the shock intensity distribution at different radial locations. Notably, the shock intensity in mid-span area is significantly reduced, which suppresses the shock wave/boundary layer interaction. Therefore, behind the shock, the boundary layer becomes thinner near the blade's trailing edge, which is associated with a decreased wake zone. These findings indicate that under upstream boundary layer ingestion conditions, the optimized sweep design effectively decreases losses from shock wave/boundary layer interaction and wake mixing.

(3) The interaction between the mainstream and tip leakage flow, as well as that between the boundary layer and shock wave, has been reduced. Thus, the optimized sweep design significantly reduces the compressor loss while enhancing its aerodynamic performance. Specifically, the adiabatic efficiency of the optimized sweep design surpasses that of the baseline design throughout the whole range of operation, while keeping the total pressure ratio. At the optimization point, a remarkable efficiency improvement of approximately 0.8% is achieved. Importantly, these improvements do not compromise the compressor's performance under clean inflow conditions. Our findings suggest that the sweep design holds considerable promise in improving the overall aerodynamic efficiency of transonic compressor rotors when operating under conditions involving upstream boundary layer ingestion.

ACKNOWLEDGEMENTS

The authors would like to give their thanks to the financial support funded by the Beijing Municipal Natural Science Foundation (No. 3242016), the National Natural Science Foundation of China (Nos. 51906005, 51976005 and 52322603), the Fundamental Research Funds for the Central Universities (Nos. 501XTCX2023146001 and YWF-23-L-1202) and the National Science and Technology Major Project (2017-II-0005-0018).

CONFLICT OF INTEREST

The authors declare no conflict of interest.

AUTHORS CONTRIBUTION

Conceptualization, **Hanan Lu** and **Tianyu Pan**; methodology, **Hanan Lu**; software, **Kaikai Shi**; validation, **Kaikai Shi**; formal analysis, **Kaikai Shi** and **Hanan Lu**; investigation, **Kaikai Shi**; resources, **Hanan Lu** and **Tianyu Pan**; data curation, **Kaikai Shi**; writing original draft preparation, **Kaikai Shi**, **Hanan Lu**, **Jian Zhang** and **Qiushi Li**; writing review and editing, **Kaikai Shi** and **Hanan Lu**; visualization, **Jian Zhang**; supervision, **Tianyu Pan**, **Hanan Lu**, **Jian Zhang** and **Qiushi Li**; project administration, **Hanan Lu** and **Tianyu Pan**; funding acquisition, **Hanan Lu** and **Tianyu Pan**. All authors have read and agreed to the published version of the manuscript.

REFERENCES

Benini, E., & Biollo, R. (2007). Aerodynamics of swept and leaned transonic compressor rotors. *Applied Energy*, *84*(10), 1012-1027. https://doi.org/10.1016/j.apenergy.2007.03.003

Bergner, J. R., Kablitz, S., Hennecke, D. K., Passrucker, H., & Steinhardt, E. (2005, June 6-9). *Influence of sweep on the 3D shock structure in an axial transonic compressor*. Proceedings of ASME Turbo Expo 2005, Reno-Tahoe, Nevada, USA. https://doi.org/10.1115/GT2005-68835

Blaha, C., Kablitz, S., Hennecke, D. K., Schmidt-Eisenlohr, U., Pirker, K., & Haselhoff, S. (2000, May 8-11). *Numerical investigation of the flow in an aft-swept transonic compressor rotor*. Proceedings of ASME Turbo Expo 2000, Munich, Germany. https://doi.org/10.1115/2000-GT-0490

Brandt, H., Fottner, L., Saathoff, H., & Stark, U. (2002, June 3-6). *Effects of the inlet flow conditions on the tip clearance flow of an isolated compressor rotor*. Proceedings of ASME Turbo Expo 2002, Amsterdam, The Netherlands. https://doi.org/10.1115/GT2002-30639

Brossman, J. R., Ball, P. R., Smith, N. R., Methel, J. C., & Key, N. L. (2014). Sensitivity of multistage compressor performance to inlet boundary conditions. *AIAA Journal of Propulsion and Power*, *30*(2), 407-415. https://doi.org/10.2514/1.B34742

Castillo Pardo, A., & Hall, C. A. (2021). Aerodynamics of boundary layer ingesting fuselage fans. *ASME Journal of Turbomachinery*, *143*(4), 041007. https://doi.org/10.1115/1.4049918

Denton, J. D. (1993). Loss mechanisms in turbomachines. *ASME Journal of Turbomachinery*, *115*(4), 621-654. https://doi.org/10.1115/1.2929299

Gil-Prieto, D., Zachos, P. K., MacManus, D. G., & McLelland, G. (2019). Unsteady characteristics of s-duct intake flow distortion. *Aerospace Science and Technology*, *84*, 938-952. https://doi.org/10.1016/j.ast.2018.10.020

Govardhan, M., Krishna Kumar, O. G., & Sitaram, N. (2007). Investigations on low speed axial compressor with forward and backward sweep. *Journal of Thermal Science*, *16*, 121-133. https://doi.org/10.1007/s11630-007-0121-3

Gümmer, V., Wenger, U., & Kau, H. P. (2001). Using sweep and dihedral to control three-dimensional flow in transonic stators of axial compressors. *ASME Journal of Turbomachinery*, *123*(1), 40-48. https://doi.org/10.1115/1.1330268

Hah, C., Puterbaugh, S. L., & Wadia, A. R. (1998, June 2-5). *Control of shock structure and secondary flow field inside transonic compressor rotors through aerodynamic sweep*. Proceedings of ASME Turbo Expo 1998, Stockholm, Sweden. https://doi.org/10.1115/98-GT-561

He, X., Fang, Z., Rigas, G., & Vahdati, M. (2021). Spectral proper orthogonal decomposition of compressor tip leakage flow. *Physics of Fluids*, *33*(10), 105105. https://doi.org/10.1063/5.0065929

Hu, J., Wang, R., & Huang, D. (2019). Improvement of performance and stability of a single-stage transonic axial compressor using a combined flow control approach. *Aerospace Science and Technology*, *86*, 283-295. https://doi.org/10.1016/j.ast.2018.12.033

Huang, S., Zhou, C., Yang, C., Zhao, S., Wang, M., & Lu, X. (2020, September 21-25). *Effect of backward sweep on aerodynamic performance of a 1.5-stage highly loaded axial compressor*. Proceedings of ASME Turbo Expo 2020, Virtual, Online. https://doi.org/10.1115/GT2020-14262

Hunter, I. H., & Cumpsty, N. A. (1982). Casing wall boundary-layer development through an isolated compressor rotor. *ASME Journal of Engineering for Gas Turbines and Power*, *104*(4), 805-817. https://doi.org/10.1115/1.3227347

Khalfallah, S., Ghenaiet, A., Benini, E., & Bedon, G. (2015). Surrogate-based shape optimization of stall margin and efficiency of a centrifugal compressor. *Journal of Propulsion and Power*, *31*(6), 1607-1620. https://doi.org/10.2514/1.B35543

Li, C., Bin, G., Li, J., Yang, P., & Wang, W. (2022). Influence of inlet distortion on the wear of aero-compressor blades. *International Journal of Mechanical Sciences*, *230*, 107551. https://doi.org/10.1016/j.ijmecsci.2022.107551

Li, F., Li, J., Dong, X., Sun, D., & Sun, X. (2017). Influence of SPS casing treatment on axial flow compressor subjected to radial pressure distortion. *Chinese Journal of Aeronautics*, *30*(2), 685-697. https://doi.org/10.1016/j.cja.2016.10.023

Li, H., Lu, H., & Li, Q. (2024). Numerical investigations of the influences of valve spool structure on the eccentric jet flow characteristic in high-pressure angle valves. *Energy*, *298*, 131378. https://doi.org/10.1016/j.energy.2024.131378

Li, J., Du, J., Geng, S., Li, F., & Zhang, H. (2020). Tip air injection to extend stall margin of multi-stage axial flow compressor with inlet radial distortion. *Aerospace Science and Technology*, *96*, 105554. https://doi.org/10.1016/j.ast.2019.105554

Li, Z., Zhang, Y., Pan, T., Lu, H., Wu, M., & Zhang, J. (2018). Optimization strategy for a single-stage axisymmetric hub endwall in axial compressor by a modified transonic area rule. *Aerospace Science and Technology*, *82*, 199-209. https://doi.org/10.1016/j.ast.2018.08.039

Lu, H., Li, Q., & Pan, T. (2018). Optimization strategy for an axial-flow compressor using a region-segmentation combining surrogate model. *Journal of Aerospace Engineering*, *31*(5), 04018076. https://doi.org/10.1061/(ASCE)AS.1943-5525.0000907

Ma, H., & Li, B. (2008). Effects of axial non-uniform tip clearances on aerodynamic performance of a transonic axial compressor. *Journal of Thermal Science*, *17*(4), 331-336. https://doi.org/10.1007/s11630-008-0331-3

Okui, H., Verstraete, T., Van den Braembussche, R. A., & Alsalihi, Z. (2013). Three-dimensional design and optimization of a transonic rotor in axial flow compressors. *ASME Journal of Turbomachinery*, *135*(3), 031009. https://doi.org/10.1115/1.4006668

Passrucker, H., Engber, M., Kablitz, S., & Hennecke, D. K. (2003). Effect of forward sweep in a transonic compressor rotor. *Proceedings of the Institution of Mechanical Engineers, Part A: Journal of Power and Energy*, *217*(4), 357-365. https://doi.org/10.1243/095765003322315414

Sasaki, T., & Breugelmans, F. (1998). Comparison of sweep and dihedral effects on compressor cascade performance. *ASME Journal of Turbomachinery*, *120*(3), 454-463. https://doi.org/10.1115/1.2841738

Scott McNulty, G., Decker, J. J., Beacher, B. F., & Khalid, S. A. (2004). The impact of forward swept rotors on tip clearance flows in subsonic axial compressors. *ASME Journal of Turbomachinery*, *126*(4), 445-454. https://doi.org/10.1115/1.1773852

Song, P., Sun, J., & Wang, K. (2014). Axial flow compressor blade optimization through flexible shape tuning by means of cooperative co-evolution algorithm and adaptive surrogate model. *Proceedings of the Institution of Mechanical Engineers, Part A: Journal of Power and Energy*, *228*(7), 782-798. https://doi.org/10.1177/0957650914541647

Strazisar, A. J., Wood, J. R., Hathaway, M. D., &Suder, K. L. (1989). Laser anemometer measurements in a transonic axial-flow fan rotor. NASA Technical Report No. 2879.

Sun, S., Wang, S., Chen, S., Tao, C., Cai, L., & Chen, J. (2019). The impact of various forward sweep angles on the performance of an ultra-high-load low-reaction transonic compressor rotor. *Applied Thermal Engineering*, *150*, 953-966. https://doi.org/10.1016/j.applthermaleng.2019.01.045

Wagner, J. H., Dring, R. P., & Joslyn, H. D. (1985a). Inlet boundary layer effects in an axial compressor rotor: Part I—Blade-to-Blade effects. *ASME Journal of Engineering for Gas Turbines and Power*, *107*(2), 374-380. https://doi.org/10.1115/1.3239734

Wagner, J. H., Dring, R. P., & Joslyn, H. D. (1985b). Inlet boundary layer effects in an axial compressor

rotor: part II—throughflow effects. *ASME Journal of Engineering for Gas Turbines and Power*, *107*(2), 381-386. https://doi.org/10.1115/1.3239735

Wang, H., Mao, X., Liu, B., Zhang, B., & Yang, Z. (2023). Effect investigation of single-slotted and double-slotted configurations on the corner separation and aerodynamic performance in a high-load compressor cascade. *Aerospace Science and Technology*, *135*, 108203. https://doi.org/10.1016/j.ast.2023.108203

Zhang, C., Hu, J., & Wang, Z. (2014). Investigations on the effects of inflow condition and tip clearance size to the performance of a compressor rotor. *ASME Journal of Engineering for Gas Turbines and Power*, *136*(12), 122608. https://doi.org/10.1115/1.4027906

Zheng, R., Xiang, J., & Sun, J. (2010, June 14-18). *Blade geometry optimization for axial flow compressor*. Proceedings of ASME Turbo Expo 2010, Glasgow, UK. https://doi.org/10.1115/GT2010-22229